Ab initio determination of anharmonic phonon peaks

Krzysztof Parlinski*
Institute of Nuclear Physics, Polish Academy of Sciences, Radzikowskiego 152, PL-31342 Kraków, Poland and Computing for Materials, PL-30150 Kraków, Poland

(Received 2 March 2018; revised manuscript received 4 June 2018; published 13 August 2018)

A method to compute anharmonic phonon peaks and anharmonic phonon-dispersion curves in crystals using *ab initio* calculated Hellmann-Feynman forces created from series of supercells is reported. The supercells are filled with atoms displaced from equilibrium positions in such a way that their configurations correspond to a given temperature. The obtained phonon-dispersion bands are able to represent the positions and shapes of the anharmonic peaks. As illustrations, the anharmonicity in cubic tungsten W, perovskite $MgSiO_3$, and superconductor MgB_2 crystals is presented. The method can be applied to search for anharmonic potential-energy landscape of crystals. It includes electron-phonon coupling.

DOI: 10.1103/PhysRevB.98.054305

I. INTRODUCTION

Handling of harmonic and anharmonic lattice dynamics is required for interesting and technologically relevant materials. These groups comprise ferroelectrics, electron-phonon mediated superconductors, and thermoelectrics, thermal conductivity materials important for the understanding of heat transfer in the Earth's interior.

The first-principle methods are reasonably accurate, and generally serve for calculation of harmonic phonon-dispersion curves. This harmonic approach is in many cases valid and useful to discuss crystal atomic vibrations. However, the studies of phenomena, which depend on anharmonic parts of the potential energy, become complex, and are still under debate.

The conventional treatment of anharmonicity in crystals relies on the expansion of the potential energy over atomic displacements up to higher-orders terms. The second-order term determines the harmonic properties, while the third-, fourth-, and higher-order expansion terms are responsible for anharmonic effects [1–5]. There exist many powerful perturbation methods [6] able to sum part of the expansion diagrams. Unfortunately, the perturbation theory tends to be computationally expensive for solids with large and complex unit cells. It is worthwhile to mention that there were approaches to supplement the conventional treatment by the self-consistent phonon theory of anharmonic lattice dynamics [7,8]. To make use of the powerful density functional theory (DFT) for treating anharmonic effects in solids several methods have been developed.

The molecular dynamics method was used to analyze the evolution of the crystal dynamics where atoms were already interacting with anharmonic potentials. In this approach, the atomic velocities, multiplied by harmonic polarization vectors and Fourier transformed to wave-vector space, define the time-dependent velocity autocorrelation function. Its time Fourier transform provides the anharmonic peaks with a Lorentzian shape [9,10]. Recently, a hybrid strategy of phonon quasiparticles from first-principle molecular dynamics simulation was proposed [11]. This method has been successfully used with the force fields [12] and DFT methods [13].

Another approach belongs to the self-consistent *ab initio* lattice dynamics (SCAILD) [14,15], and the stochastic self-consistent harmonic approximation (SSCHA) [16], which can incorporate the effect of lattice anharmonicity at the mean-field level. A further approach relies on the temperature-dependent effective potential (TDEP) method, in which effective harmonic and cubic force constants are extracted from displace-force data calculated for an atomic configuration sampled by *ab initio* molecular dynamics (AIMD) [17,18]. In comprehensive reviews [16,19], elegant formulations of self-consistent phonon (SCP) theory, based on the many-body theory [20], can be found. But even in the case of the simplest solution, which would allow us to derive the effective anharmonic phonon frequency, it is required to know the fourth-order anharmonic force constants, or their substitutes. Several additional methods, which consider crystal anharmonicity, have been reported in Refs. [21–23].

In this paper a method is proposed to handle anharmonicity in crystals including larger crystals unit cells within a non-perturbative method. It relies on probing the potential-energy landscape of the crystal in the multidimensional space of atomic displacements. Then, the vibrations are transformed and classified in the wave vector reciprocal space, similar to the harmonic case. The expansion of the potential energy is not involved. The method permits us to determine the harmonic and anharmonic phonons using the *ab initio* technique. Below, we present three examples as an illustration of the method. These illustrative examples show that the approach is able to include to the anharmonicity effects of phonon-phonon and electron-phonon couplings. However, it should be stated that in this paper phenomena such as soft modes, unstable modes, etc., are not treated. Here, we consider anharmonic systems where self-consistent lattice dynamics is not involved.

*krzysztof.parlinski@ifj.edu.pl

II. METHOD

The conventional harmonic phonon theory uses an approximation, which assumes that atoms interact via harmonic force constants. Such harmonic force constants do not change with the amplitude of a displaced atom. Then, from the crystal symmetry follows the symmetry constraints obeyed by force constants and possible invariances. The assumption that phonons are infinite waves of collective atom vibration allows us to represent phonons in the reciprocal space and express them as phonon-dispersion curves in the $(\omega, \mathbf{k})$ space. A dispersion curve can be considered as the density of harmonic phonons. Each point of this density may be treated as the δ function intensity distributed over the $(\omega, \mathbf{k})$ space. The δ functions are measured, for example, in a coherent scattering experiment. Moreover, the knowledge of polarization vectors, obtained while diagonalizing the dynamical matrix, defines the phonon mode symmetry, and determines the contribution of specific atom vibrations to a given phonon mode. The computational method [24] allows us to calculate harmonic phonons using small atomic displacements, so small that the atomic amplitudes remain in the harmonic regime.

In this paper a similar strategy is proposed for presenting the anharmonic phonon-dispersion curves in the $(\omega, \mathbf{k})$ space. The essential difference is that anharmonic modes are characterized by peaks having certain shapes and widths. Hence, instead of plotting δ-function phonon-dispersion curves, one should plot, in the $(\omega, \mathbf{k})$ space, anharmonic phonon-dispersion bands. The section of each band across $\mathbf{k} = \text{const}$ represents a set of anharmonic phonon peaks. Using symmetry properties of the overlayed peaks one can decouple them into individual peaks.

In this paper for anharmonic phonon-dispersion bands a method similar to the harmonic one formulated in Ref. [24] is used. However, to obtain particular phonon-dispersion curves, one should use an atomic configuration, in which all atoms in the crystal (supercell) could be displaced, and their displacement amplitudes could have entered already the anharmonic regime. Such particular anharmonic phonon-dispersion curves will slightly differ from the harmonic plot. Making a series of such particular runs, and gathering the resulting dispersion curves, one gets the anharmonic phonon-dispersion bands. The atomic configuration should be determined according to such rules, which reflect in the best way the displaced position of atoms in the crystal, being at a desired temperature T. One option of such rules is proposed below in Sec. II B.

The plot of the anharmonic phonon-dispersion bands could be considered as a landscape, or distribution of phonon frequencies over the whole $(\omega, \mathbf{k})$ space, a distribution which characterizes the anharmonic crystal. Moreover, the symmetry relations included in polarization vectors allow us to carry out detailed discussion on the particular anharmonic peak, its relation to other harmonic modes, contributions of atoms to its intensity, etc. This method needs to know the forces acting between the atoms, but it does not need to expand the potential energy over atomic displacements. The current method is similar to the self-consistent phonon SCP method [19], which is applied to soft mode. However, effects related to soft modes are not discussed below.

The existing DFT codes provide sufficiently accurate Hellmann-Feynman (HF) forces for any atomic configuration, and are able to establish force constants to calculate the phonon frequencies and phenomena related to the atomic vibrations. The DFT approach requires us to approximate the crystal as a *supercell*, with periodic boundary conditions imposed. The computations perform first the optimization of the supercell structure, and then data for crystal dynamical properties such as phonons are derived.

A. Harmonic phonons

To compute *harmonic* phonons, the *ab initio* force constant approach formulated by Parlinski, Li, and Kawazoe in 1997 [24] can be used. This method has been already applied to about a thousand crystals, crystals with surfaces, defects, etc., and the results generally show good agreement with the measured phonon data. As an input, the HF forces $\mathbf{F}_H(\mathbf{n}, \mu)$ computed by the DFT code are imported. The procedure relies on using the relation between harmonic forces $\mathbf{F}_H(\mathbf{n}, \mu)$, induced by atoms displaced by $\mathbf{U}(\mathbf{m}, \nu)$ from the equilibrium position [25],

$$\mathbf{F}_H(\mathbf{n}, \mu) = -\sum_{\mathbf{m},\nu} \mathbf{B}_H(\mathbf{n}, \mu; \mathbf{m}, \nu) \cdot \mathbf{U}(\mathbf{m}, \nu), \tag{1}$$

where $\mathbf{n}$, $\mathbf{m}$ label primitive unit cells in the supercell, and μ, ν are indices of atoms. The $\mathbf{B}_H(\mathbf{n}, \mu; \mathbf{m}, \nu)$ are 3×3 harmonic force constant matrices, having nine elements, which are also called parameters. They determine the conventional dynamical matrix [26] as

$$\mathbf{D}(\mathbf{k}; \mu, \nu) = \frac{1}{\sqrt{m_\mu m_\nu}} \sum_{\mathbf{m}} \mathbf{B}_H(0, \mu; \mathbf{m}, \nu) \times \exp\{-2\pi \mathbf{k} \cdot [\mathbf{R}(0, \mu) - \mathbf{R}(\mathbf{m}, \nu)]\}, \tag{2}$$

where m_μ, m_ν are masses of atoms. Its eigenvalue equation

$$\omega^2(\mathbf{k}, j)\mathcal{E}(\mathbf{k}, j) = \mathbf{D}(\mathbf{k})\mathcal{E}(\mathbf{k}, j) \tag{3}$$

provides phonon frequencies $\omega^2(\mathbf{k}, j)$, and eigenvectors $\mathcal{E}(\mathbf{k}, j)$.

In Ref. [24], it was proposed to decouple each force constant matrix into a product

$$\mathbf{B}_H(\mathbf{n}, \mu; \mathbf{m}, \nu) = \mathbf{A}(\mathbf{n}, \mu; \mathbf{m}, \nu) \cdot \mathbf{P}_H(\mathbf{n}, \mu; \mathbf{m}, \nu), \tag{4}$$

where the $\mathbf{A}(\mathbf{n}, \mu; \mathbf{m}, \nu)$ matrix is entirely determined by crystal symmetry. The $\mathbf{P}_H(\mathbf{n}, \mu; \mathbf{m}, \nu)$ matrix depends on potential parameters only. This relationship follows from the point-group symmetry of the bond contained in $\mathbf{B}_H(\mathbf{n}, \mu; \mathbf{m}, \nu)$, it means the bond between the $(\mathbf{n}, \mu)$ and the $(\mathbf{m}, \nu)$ atoms [26]. Constructing the projection operator from the bond point group one arrives at the $\mathbf{A}(\mathbf{n}, \mu; \mathbf{m}, \nu)$ matrix. Hence it also follows how many independent parameters determine a given force constant. Using Eq. (4), Eq. (1) becomes

$$\mathbf{F}_H(\mathbf{n}, \mu) = \sum_{\mathbf{m},\nu,j} \mathbf{C}_U(\mathbf{n}, \mu; \mathbf{m}, \nu) \cdot \mathbf{P}_H(\mathbf{n}, \mu; \mathbf{m}, \nu), \tag{5}$$

where the matrix

$$\mathbf{C}_U(\mathbf{n}, \mu; \mathbf{m}, \nu) = -\mathbf{U}(\mathbf{m}, \nu) \cdot \mathbf{A}(\mathbf{n}, \mu; \mathbf{m}, \nu) \tag{6}$$

is known, because one knows the used atomic displacements and crystal symmetry elements collected in the bond point groups. The symmetry matrix imposes constraints on the values of the force constant parameters $\mathbf{P}_H(\mathbf{n}, \mu; \mathbf{m}, \nu)$. As

a result a number of independent and unknown parameters $\mathbf{P}_H(\mathbf{n}, \mu; \mathbf{m}, \nu)$ becomes smaller than the number of available forces $\mathbf{F}_H(\mathbf{n}, \mu)$. In turn, the forces $\mathbf{F}_H(\mathbf{n}, \mu)$ are directly computed in the *ab initio* run, by the displacing single nonequivalent atom, and relaxing the electronic states only. The forces arise from a displacement $\mathbf{U}(\mathbf{m}, \nu)$ of a single atom. A run in a supercell provides $3n$ HF forces, where n is the number of atoms in the supercell. Such a set of HF forces is called a *force list*. A minimum number s of HF force lists is equal to the number of nonequivalent atoms of a primitive unit cell, multiplied by a number of nonequivalent directions of displacements of each nonequivalent atom.

Equation (5) can be written in the matrix form as

$$\mathcal{F}_\mathcal{H} = \mathcal{C}_\mathcal{U} \cdot \mathcal{P}_\mathcal{H}. \tag{7}$$

It presents a *global form* of the system of $3ns$ equations for the harmonic force constant parameters $\mathcal{P}_\mathcal{H}$, which must be solved simultaneously. Here, F_H, C_U, P_H are $(3ns\times 1)$, $(3ns\times p')$, $(p'\times 1)$ dimensional matrices, respectively, and p' is the total number of independent potential parameters of all force constants within the supercell. Due to applied symmetry elements, in this system the number of HF forces exceeds the number of potential parameters, $3ns > p'$, therefore, Eq. (7) is an *overdetermined* system. To solve it [24], the singular value decomposition method (SVD) [27] was applied to the C_U matrix. This SVD method provides a solution, which is the best approximation of $\mathcal{P}_\mathcal{H}$ to $\mathcal{F}_\mathcal{H}$ in the *least-square sense*.

Moreover, the invariance of the potential energy against translation of all crystal atoms by constant vector $\mathbf{S}$, i.e., $\mathbf{U}(\mathbf{m}, \nu) \to \mathbf{U}(\mathbf{m}, \nu) + \mathbf{S}$, requires that

$$\sum_{\mathbf{m},\nu} \mathbf{B}_H(\mathbf{n}, \mu; \mathbf{m}, \nu) = 0. \tag{8}$$

Equation (8) guarantees that the acoustic-phonon modes have zero frequency at reciprocal Γ points. This relation was also used in the past [2,26] to determine the parameters of the on-site force constants $\mathbf{B}_H(0, \mu; 0, \nu)$. Unfortunately, the number of unknown parameters of the on-site force constant could be different from the number of relations provided by Eq. (8), and then the invariance Eq. (8) could not be automatically obeyed. The solution requires to apply the SVD method. As a rule, violation of Eq. (8) occurs for more complex crystals.

Similarly, from the invariance of potential energy against infinitesimal crystal rotation follows the next constraint, which reads

$$\sum_{\mathbf{m},\nu} \{B_{H,i,j}(\mathbf{n}, \mu; \mathbf{m}, \nu) R_k(\mathbf{m}, \nu) - B_{H,i,k}(\mathbf{n}, \mu; \mathbf{m}, \nu) R_j(\mathbf{m}, \nu)\} = 0, \tag{9}$$

where $\mathbf{R}(\mathbf{m}, \nu)$ indicates the equilibrium position of the $(\mathbf{m}, \nu)$ atom. The symmetry, translational, and rotational invariances deliver constraints on the number and magnitudes of independent parameters of force constants. All these constraints could be included into the *global form*, Eq. (7). The two invariances, Eqs. (8) and (9), can be written as a matrix M of $(18n\times p')$ dimensions, which act on $\mathbf{P}_H(\mathbf{n}, \mu; \mathbf{m}, \nu)$. Then

$$\begin{pmatrix} \mathcal{F}_\mathcal{H} \\ 0 \end{pmatrix} = \begin{pmatrix} \mathcal{C}_\mathcal{U} \\ \beta\mathcal{M} \end{pmatrix} \cdot \mathcal{P}_\mathcal{H}. \tag{10}$$

Here, β adjusts the strength of the translational-rotational invariances. In very simple crystal structures, the derived force constants always fulfill the above invariances. Then, $\beta = 0$ can be set. For complex crystals, or DFT studies of complicated supercells, such as surfaces, which suffer from some numerical noise, the invariances might not be satisfied, then one may force to fulfill them by adjusting $\beta > 0$. Physically, of course, the symmetry has priority, with respect to small modifications of the force-constant parameters. Then, the above described procedure, using again SVD, provides an effective method to find harmonic phonons, their frequencies, eigenvectors, phonon-dispersion curves, phonon density of states, and other phonon dependent quantities, which obey the symmetry of the crystal, and translational and rotational invariances.

It is useful to understand the physical features of the above method. The phonon calculations are performed at a supercell, on which periodic boundary conditions are always imposed. Such circumstances involve limitations on the accuracy of the calculated phonons. However, there are the following rules: (i) If the interaction range is confined to the *supercell interior*, then all phonon frequencies are exact. (ii) If the interaction range exceeds the supercell size, then nevertheless there are exact phonon frequencies, which occur for *exact* discrete wave vectors $\mathbf{k}_s$. The discrete wave vectors must be commensurate with the supercell size. It follows from the form of the dynamical matrix, Eq. (2), that the exact wave vectors $\mathbf{k}_s$ must fulfill the following conditions: $\exp\{-2\pi\mathbf{k}_s \cdot \mathbf{a}_i^{(SC)}\} = 1$, where $\mathbf{a}_i^{(SC)}$ are the lattice constants of the supercell, and $i = 1, 2, 3$. The phonon frequencies beyond the exact wave vectors are interpolations between the $\mathbf{k}_s$ points. Of course, the used symmetry also determines the force constants, and this helps us to obtain such phonon-dispersion curves, which resemble the real ones.

B. Anharmonic phonons

To compute *anharmonic* effects one may use a similar approach as above. Any DFT calculations of HF forces contain information on the anharmonicity. This means that there is an access to anharmonic landscape of the crystal potential energy. Moreover, the anharmonic potential may involve a lot of atoms displaced simultaneously. During time, the atoms vary displacements around equilibrium positions. Making a snapshot at a fixed time moment, one might see that all atoms of a supercell form a displacement pattern (DP) $\mathbf{U}^{(i)}$, where each pattern will be indexed by (i). Some displacements of $\mathbf{U}^{(i)}(\mathbf{n}, \mu)$ might exceed the harmonic region. One may treat also DP (i) as coming from different locations of the crystal. Using DFT, each DP (i) allows us to calculate one HF force list $\mathbf{F}_A^{(i)}$ with anharmonic contributions. Each such run involves the relaxation of the electronic states only.

Knowing the displacements $\mathbf{U}^{(i)}$ and force lists $\mathbf{F}_A^{(i)}$, we supplement Eq. (10) with the anharmonic contributions, formulating in this way *a global anharmonic form* of a system of equations,

$$\begin{pmatrix} \mathcal{F}_\mathcal{H} \\ 0 \\ \mathcal{F}_\mathcal{A}{}^{(i)} \end{pmatrix} = \begin{pmatrix} \mathcal{C}_\mathcal{U} \\ \beta\mathcal{M} \\ \mathcal{C}_{U^{(i)}} \end{pmatrix} \cdot \mathcal{P}_\mathcal{A}{}^{(i)}, \tag{11}$$

where $\mathbf{C}_{U^{(i)}}(\mathbf{n}, \mu; \mathbf{m}, \nu)$ is determined by a relation similar to Eq. (6), and $i = 1, 2, \ldots N$ runs over DP's. This system of equations is formulated in the spirit of the perturbation theory of the singular value decomposition [28]. Now, a single SVD solution of Eq. (11), corresponding to one DP, gives a single set of dispersion curves with the index (i). Again, the SVD method ensures the best least-square approximation of parameters $\mathcal{P}_{\mathcal{A}}{}^{(i)}$ to both force lists $\mathcal{F}_{\mathcal{H}}$ and $\mathcal{F}_{\mathcal{A}}{}^{(i)}$. Now, the parameters $\mathcal{P}_{\mathcal{A}}{}^{(i)}$ do not correspond to an ideal harmonic crystal, but determine the forces acting between the atoms displaced from equilibrium positions in accordance to the used DP. Therefore, they can describe anharmonic effects. The above approach goes along a similar line as the general idea developed in the field of information science for recording sparse solutions [29] and later suggested to be used for lattice dynamics [30].

For a realistic modeling of anharmonic effects one should select a sequence of N independent DP's ($i = 1, 2, \ldots N$), and compute dispersion curves for *all* these N patterns. From one DP to another DP, probing different anharmonic environments, the phonon-dispersion curves are slightly different due to variation of potential energy created by displaced atoms. In the absence of anharmonicity, and with negligible atomic amplitudes, all phonon-dispersion curves will be identical to the harmonic case. However, in the anharmonic case, all phonon-dispersion curves, $i = 1, 2, \ldots N$ form rather *phonon bands* of finite widths.

Again, every single atomic configuration DP is a perturbation in Eq. (11). Its solution tells us about the modifications of the (i) set of phonon-dispersion curves. The modified phonon-dispersion curves can be treated as energy characteristics of the atomic configuration (i). Every other atomic configuration (i) provides another set of phonon-dispersion curves, or energy characteristics. For a given size of supercell we should use all phonons allowed by this size, varying only phonon wave phases. The accuracy may be improved by applying larger supercells, since then more kinds of commensurate phonon waves can be inserted into the supercell.

To stay consistent with the supercell concept, DP's $\mathbf{U}^{(i)}$ must preserve the periodic boundary conditions. Thus, a DP must be generated as a superposition of the allowed phonon-displacement waves. It means that each phonon-displacement wave must be commensurate with the supercell size and shape. At the end of Sec. II A, when the harmonic exact phonon-dispersion curves were discussed, the same principles have already been used. There, accurate phonon frequencies have been obtained for exact commensurate wave vectors $\mathbf{k}_s$. A similar approach is applied here to select exact displacement waves. The amplitudes of these waves can be estimated from the harmonic theory as

$$\mathbf{U}(\mathbf{n}, \mu) = \frac{Q(\mathbf{k}, j)}{\sqrt{m_\mu}} \mathcal{E}(\mathbf{k}, j) \exp\{2\pi i[\mathbf{k} \cdot \mathbf{R}(\mathbf{n}, \mu) - \phi(\mathbf{k}, j)]\}, \tag{12}$$

where one may vary randomly also the phonon phases $\phi(\mathbf{k}, j)$. The $Q(\mathbf{k}, j)$ is taken from its mean-square amplitude,

$$\langle Q^2(\mathbf{k}, j)\rangle = \frac{\hbar}{2\omega(\mathbf{k}, j)} coth\left(\frac{\hbar\omega(\mathbf{k}, j)}{2k_B T}\right), \tag{13}$$

where $\omega(\mathbf{k}, j)$ and $\mathcal{E}(\mathbf{k}, j)$ are the harmonic phonon frequencies and polarization vectors, respectively, at wave vector $\mathbf{k}$, and phonon branch j. Here, T is the temperature at which the crystal anharmonicity is studied. The temperature displacements in Eq. (12) depend on the thermal occupation factor, Eq. (13). The proposed phonon waves with varying phases leads, in the limit of a large supercell, and in harmonic approximation, to Gaussian displacements probability distribution on every crystal site. The width of the corresponding Gaussian is determined by the mean-square displacement related to atoms located at the considered site [31]. This theorem was formulated by Debye in classical [32] cases and by Ott in quantum [33] cases. It tells us how the crystal is filled with harmonic phonon waves. Here, according to our approximation, in the supercell only phonons of commensurate wavelengths are generated.

The DP's may also be obtained as snapshots of atomic motion traced during molecular dynamic simulation at a specific temperature T. Also in this case, phonon waves are commensurate with the supercell size.

For the same wave vector $\mathbf{k}$ the anharmonic phonon bands frequently overlap. Therefore, we found a systematic *projection method* to select out any single anharmonic peak from the whole phonon band. A diagonalization of the dynamical matrix, Eq. (2), delivers orthonormalized eigenvectors $\mathcal{E}^{(0)}(\mathbf{k}, J)$ of harmonic phonon curves, where J labels phonon modes for the same wave vector $\mathbf{k}$. Similarly, one obtains the $\mathcal{E}^{(i)}(\mathbf{k}, j)$ eigenvectors of the anharmonic phonon bands, relevant for all DP's (i), where j label phonon modes for the same wave vector $\mathbf{k}$. Each eigenvector involved in the anharmonic peak can be expanded over a complete set $J = 1, 2, \ldots J_{\max}$ of harmonic eigenvectors,

$$\mathcal{E}^{(i)}(\mathbf{k}, j) = \sum_{J=1}^{J_{\max}} \alpha^{(i)}(\mathbf{k}, j, J) \mathcal{E}^{(0)}(\mathbf{k}, J). \tag{14}$$

Applying the orthonormality relation $\sum_{\mathbf{j}=1}^{j_{\max}} \mathcal{E}^{*(i)}(\mathbf{k}, j) \cdot \mathcal{E}^{(i)}(\mathbf{k}, j) = 1$, the expansion coefficients of Eq. (14) can be found as $\alpha^{(i)}(\mathbf{k}, j, J) = \mathcal{E}^{*(i)}(\mathbf{k}, j) \cdot \mathcal{E}^{(0)}(\mathbf{k}, J)$.

The total density of anharmonic states $b(\omega, \mathbf{k})$ for the fixed $\mathbf{k}$ wave vector is

$$b(\omega, \mathbf{k}) = \frac{1}{Z} \sum_{i=1}^{N} \sum_{j=1}^{j_{\max}} \delta_{\Delta\omega}[\omega - \omega^{(i)}(\mathbf{k}, j)], \tag{15}$$

where the constant $Z = N J_{\max} j_{\max} \Delta\omega$. The histogram bin $\Delta\omega$ is defined by the function $\delta_{\Delta\omega}(x) = 1$, if $-\frac{\Delta\omega}{2} < x \leqslant \frac{\Delta\omega}{2}$, or 0 otherwise. For fixed $\mathbf{k}$ the $b(\omega, \mathbf{k})$ can be plotted as single spectrum of ω. For a set of parallel $\mathbf{k} = \text{const}$ lines on the $(\omega, \mathbf{k})$ plane the amplitudes $b(\omega, \mathbf{k})$ can be converted to colors and plotted as a map, where the colors denote the amplitude of $b(\omega, \mathbf{k})$.

At fixed $\mathbf{k}$ wave vector, *the density of states for the anharmonic peak of mode* J, denoted by $b_J(\omega, \mathbf{k})$, as a function of frequency ω, can be found from the histogram

$$b_J(\omega, \mathbf{k}) = \frac{1}{Z} \sum_{i=1}^{N} \sum_{j=1}^{j_{\max}} |\alpha^{(i)}(\mathbf{k}, j, J)|^2 \delta_{\Delta\omega}[\omega - \omega^{(i)}(\mathbf{k}, j)]. \tag{16}$$

The coefficients $\alpha^{(i)}(\mathbf{k}, j, J)$ select out from all the bands (i) only those phonon intensities which resemble the vibrations determined by harmonic eigenvectors $\mathcal{E}^{(0)}(\mathbf{k}, J)$. Each $b_J(\omega, \mathbf{k})$ determines *a single anharmonic peak* of symmetry J and wave vector $\mathbf{k}$. This method can sort out all anharmonic peaks, even if they overlap.

The crystal symmetry is determined by the crystallographic space group. Hence, an irreducible representation of the crystallographic space group is assigned to each harmonic phonon mode. The present method assures that the irreducible representations of all phonon modes belonging to the same phonon band are the same. Therefore, a given anharmonic phonon peak is characterized by the same irreducible representation as the corresponding harmonic phonon peak. Thus, the conventional assignment of harmonic phonon modes is accepted as a reference to classify the anharmonic peaks.

III. ILLUSTRATIVE EXAMPLES

The above method was applied to three examples, namely a crystal of tungsten W, a mineral $MgSiO_3$, and a BCS superconductor MgB_2. The calculations were performed on the respective supercells using the VASP software [34], and applying the generalized gradient approximation (GGA)–projector augmented wave (PAW) approach issued with this code. Each unit cell and subsequently supercell were relaxed to the ground-state stable structure, at which all HF forces acting on all atoms of the supercell vanish. The harmonic force constants and phonons were calculated with the PHONON software [35], according to Eq. (10), taking into account the symmetry of the crystal space group. Next, sets of DP's were generated using the amplitude of displacements as suggested by Eqs. (12) and (13). Each HF force list provided phonon-dispersion curves, which might have been more or less different from the harmonic one. Indeed, the atomic configuration in the supercell resembles the fluctuation occurring at a finite temperature in the crystal, therefore in a nonharmonic potential the phonon frequencies in such an environment might be different. An average over all computed phonon-dispersion curves gave a number of quantities, which characterize the crystal anharmonic properties. Among these properties are the anharmonic phonon intensity maps, which are graphic representations of the anharmonic phonon-dispersion bands. All maps were created so that the phonon frequencies at a fixed wave vector were sorted to bins of a histogram, and a color index was assigned to the number of collected frequencies in the bin. The color scales of all maps presented here go from the lowest (black) to highest (red) colors. The histograms were analyzed by the orthonormalized polarization vectors for the same wave vector according to the rule Eq. (16), to separate phonon peaks of different symmetries. Such an analysis can be done in the PHONONA software, which generates DP files and solves the global anharmonic form system Eq. (11).

A. Tungsten W

Tungsten W crystallizes in the bcc cubic structure with the space group $Im\bar{3}m$. The *ab initio* calculations were carried on a $2\times2\times2$ supercell with 16 atoms and using a $4\times4\times4$ k mesh. The optimized lattice constant was $a = 3.171$ Å. Harmonic

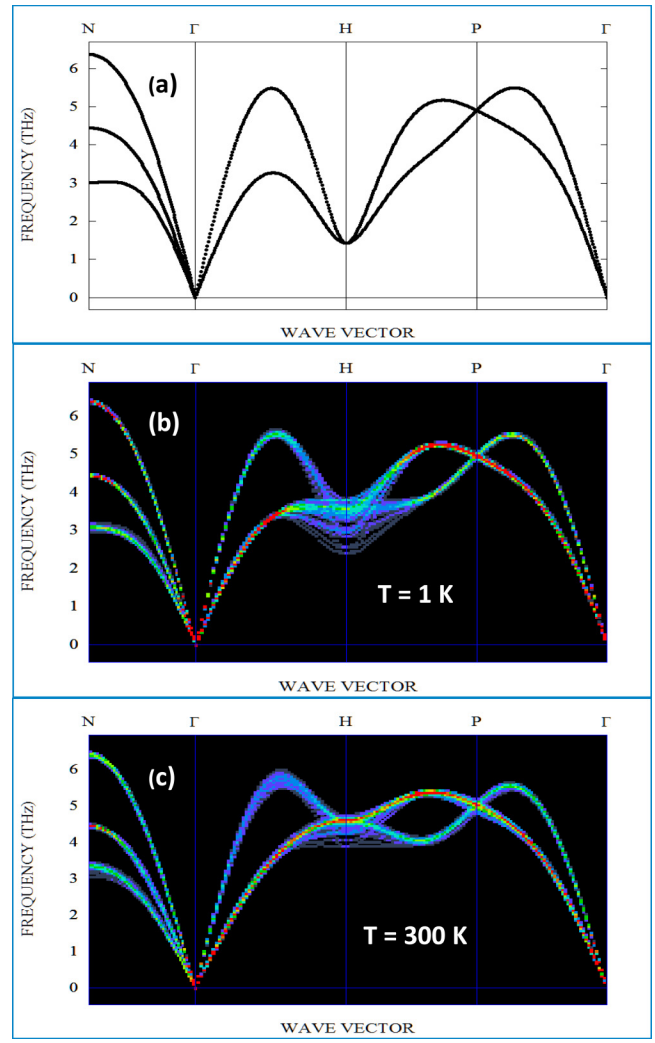

FIG. 1. Tungsten W phonon-dispersion curves along N-Γ-H-P-Γ wave-vector path. (a) Harmonic dispersion relations. (b),(c) Anharmonic phonon maps created from averaging over 50 different sets of DP's at $T = 1$ K and $T = 300$ K, respectively.

phonon-dispersion curves are shown in Fig. 1(a). Next, for 15 temperatures from 1 to 4200 K in intervals of 300 K, 50 DP's were generated for each temperature. The used mean displacement amplitudes $\bar{X} = \sqrt{\langle U_x U_x \rangle}$ for $1, 300, \ldots, 4200$ K were on average equal to $0.0265, 0.0319, \ldots, 0.1732$ Å, respectively. For each temperature the 50 DP's provided 50 force-constant lists by using Eq. (11). The results of elaborating all 50 lists of force constants led to maps of phonon-dispersion bands, which for $T = 1$ K and $T = 300$ K are plotted at Figs. 1(b) and 1(c). One can see that at $T = 1$ K phonon widths are negligible, except for the triply degenerate mode at the H high-symmetry point of the Brillouin zone. A convergence test for 300 DP's provided a smooth and elegant asymmetric phonon peak with the same linewidth as the relevant peak found from 50 DP's.

The phonon-dispersion curves were measured at $T = 300$ K by coherent neutron-scattering spectroscopy [36,37]. The measurements [37] included also the anharmonic frequency linewidths at the H wave vector in order to observe

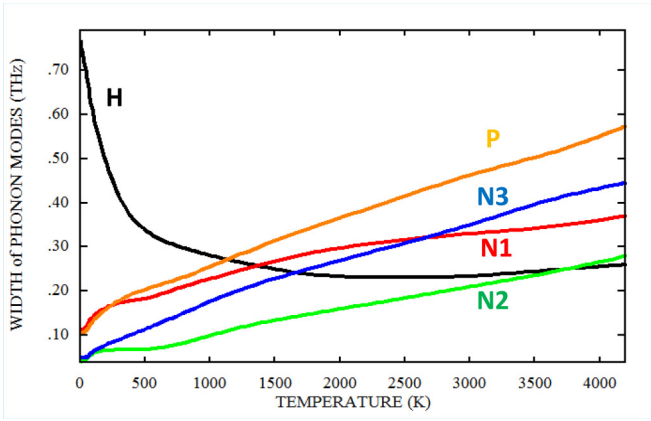

FIG. 2. The phonon linewidth temperature behaviors of phonons in bcc cubic tungsten. The labels $N1$, $N2$, $N3$ (from lowest to higher frequency at $\mathbf{k} = N$), H, and P denote the high-symmetry points of bcc Brillouin zone. The phonon mode at H point has large linewidth, which diminishes while decreasing the temperature.

phonon behavior close to the predicted Kohn effect [38]. Unfortunately, as follows from Ref. [37] the Kohn effect could not be unambiguously observed. The phonon-dispersion curves were recently calculated using the first-principle method SCAILD [15]. There, at $T = 300$ K the renormalized phonon frequency at the H wave vector was 5.5 THz. The present harmonic phonon frequency at the H point occurs at 1.5 THz, while at $T = 300$ K the anharmonic mechanism elevates it to 4.7 THz [Fig. 1(c)].

Moreover, Figs. 1(b) and 2 suggest that at the H high-symmetry point, the highest linewidth occurs at low temperature, and the width diminishes with increasing temperature. The linewidth broadening could be a sign of a strong electron-phonon coupling at the H points. It is worth noticing that the linewidths of remaining phonon peaks belonging to other high-symmetry points always increase with temperature (Fig. 2). Searching at $T = 1$ K for a wide phonon linewidth beyond the H points of the Brillouin zone was unsuccessful. Moreover, W becomes a superconductor below 0.015 K, and the electron-phonon coupling seems to be responsible for the superconducting property, according to the conclusions of Ref. [39].

B. Magnesium Silicate $MgSiO_3$

The anharmonicity of $MgSiO_3$ has been studied in Refs. [10,11,13,40] with respect to thermodynamic properties and thermal conductivity of the Earth's lower mantle. The perovskite $MgSiO_3$ belongs to the orthorhombic space group $Pmnb$, no. = 62. The crystal structure lattice parameters have been measured [41–43] and optimized with the DFT code [44].

We have selected for *ab initio* runs the $1\times\sqrt{2}\times\sqrt{2}$ supercell, and $2\times2\times2k$-point mesh. For illustration, two unit cells under hydrostatic pressure of $P = 57.3$ GPa and $P = 0.0$ GPa were prepared. The structure DFT optimization started from parameters given in [44]. The lattice constants of the primitive unit cells were $a = 6.481$ Å, $b = 4.689$ Å, $c = 4.462$ Å, and $a = 6.840$ Å, $b = 4.904$ Å, $c = 4.743$ Å. From these cells two supercells were built. Inserting to supercells the DP's, Eqs. (12) and (13), we could simulate temperatures $T = 2300$ K and $T = 800$ K. With inserted DP's the pressures increased to $P = 70.5$ GPa and $P = 0$ GPa, respectively. Then, for each supercell 100 DP's were generated. The primitive unit cell contains 20 atoms, therefore 60 phonon-dispersion curves exist. The harmonic phonon-dispersion curves plotted along the Γ-X-S-Y-Γ-Z-U-R-T-Z wave vectors are shown on Fig. 3(a). For the above given temperatures and pressures the used mean displacements of atoms were $\bar{X}_{Mg} = 0.127$ Å, $\bar{X}_{Si} = 0.087$ Å, $\bar{X}_{O1} = 0.110$ Å, $\bar{X}_{O2} = 0.105$ Å, and $\bar{X}_{Mg} = 0.099$ Å, $\bar{X}_{Si} = 0.063$ Å, $\bar{X}_{O1} = 0.087$ Å, $\bar{X}_{O2} = 0.075$ Å, respectively.

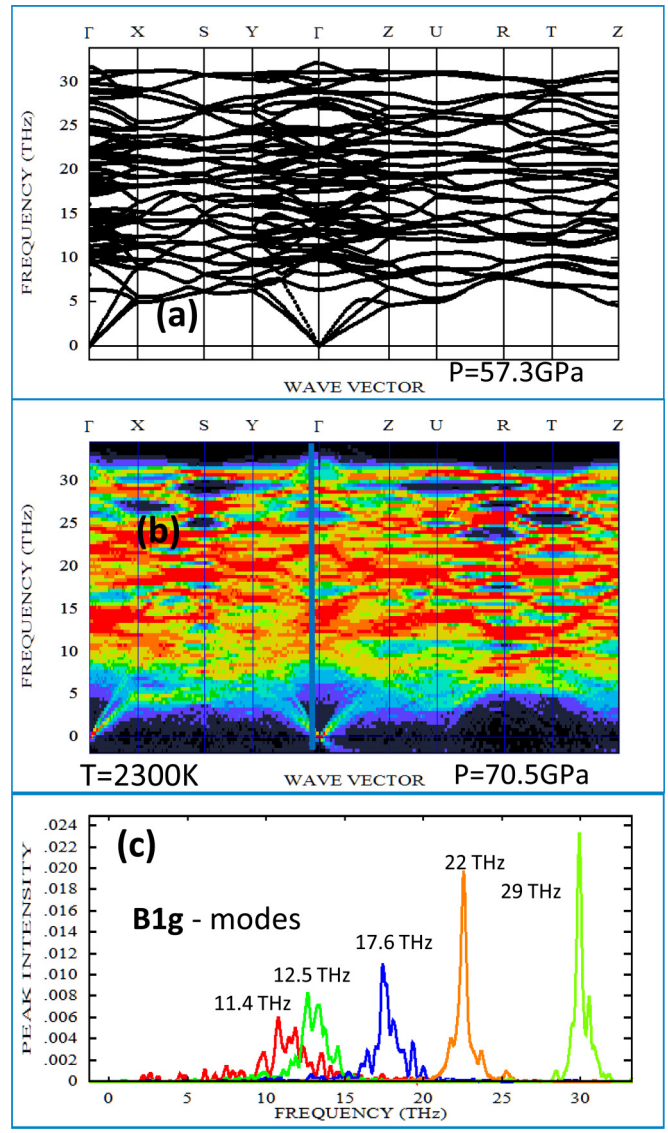

FIG. 3. $MgSiO_3$ phonon-dispersion curves along Γ-X-S-Y-Γ-Z-U-R-T-Z wave-vector path. (a) Harmonic phonon-dispersion relations at temperatureless regime, and pressure $P = 57.3$ GPa. (b) Anharmonic phonon bands created by 100 different sets of DP's at $T = 2300$ K and $P = 70.5$ GPa. (c) Plots of all anharmonic peaks of B_{1g} symmetry close to $\mathbf{k} = \Gamma(0, 0, 0)$ [close to vertical line at (b)].

Within the two considered states of $MgSiO_3$, the anharmonic properties were studied. The harmonic phonon-dispersion curves, Figs. 3(a) and 4(a) do not show soft modes.

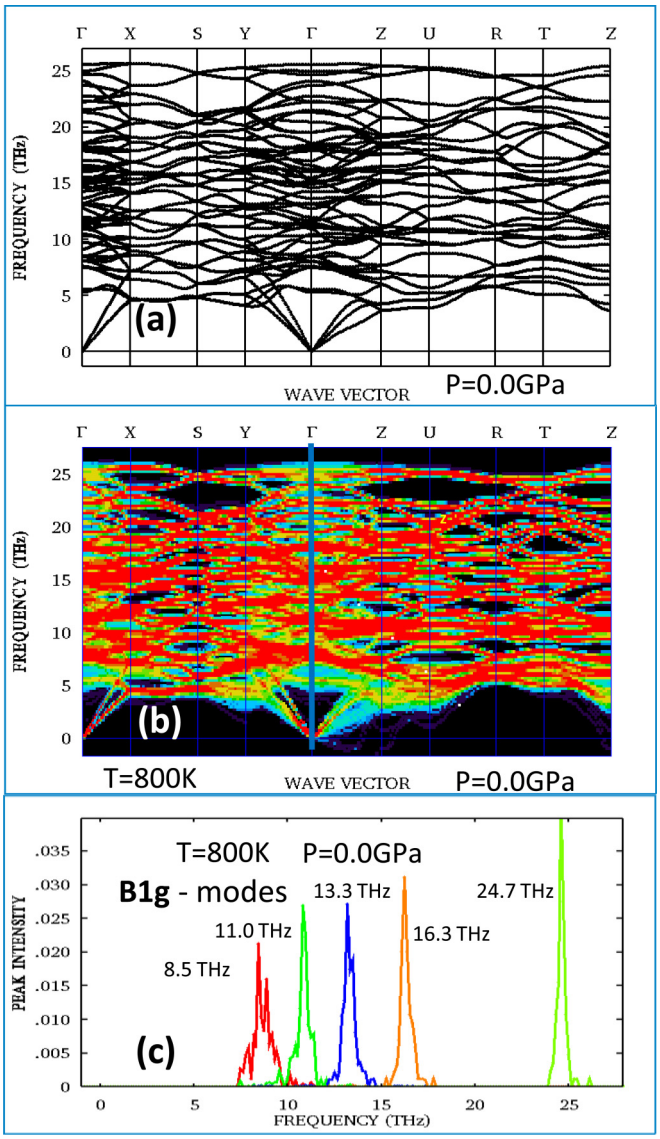

FIG. 4. $MgSiO_3$ phonon-dispersion curves along Γ-*X*-*S*-*Y*-Γ-*Z*-*U*-*R*-*T*-*Z* wave-vector path. (a) Harmonic phonon-dispersion relations at temperatureless regime, and pressure $P = 0.0$ GPa. (b) Anharmonic phonon bands created by 100 different sets of DP's at $T = 800$ K and $P = 0.0$ GPa. (c) Plots of all anharmonic peaks of B_{1g} symmetry close to $\mathbf{k} = \Gamma(0, 0, 0)$ [close to vertical line at (b)].

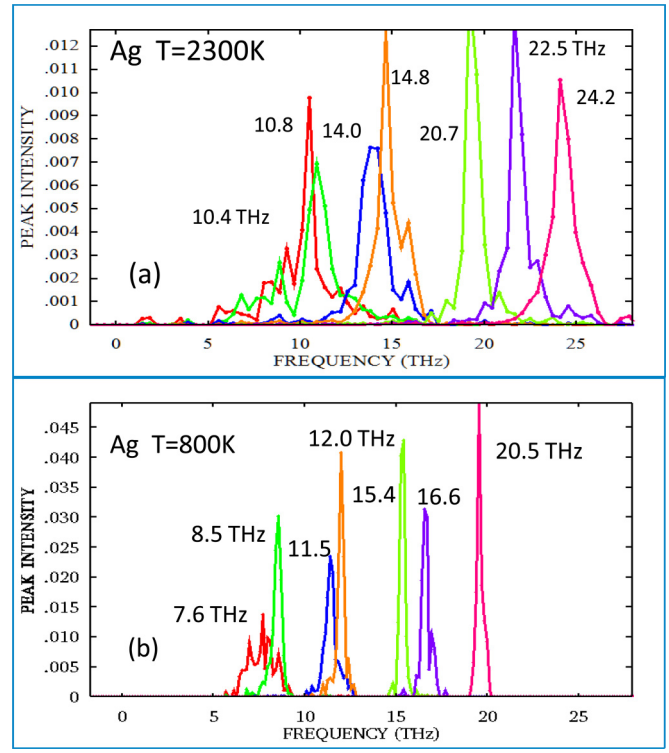

FIG. 5. A comparison of A_g anharmonic phonon modes of $MgSiO_3$ at Γ wave vector. (a) at $T = 2300$ K and $P = 70.5$ GPa, (b) at $T = 800$ K and $P = 0.0$ GPa. No smoothing is used for plots. The lines joint the points following from the histograms created by 100 different sets of DP's.

The maximum phonon frequency at 34 and 27 THz correspond to pressures $P = 57.3$ GPa and $P = 0.0$ GPa, respectively. Figures 3(b) and 4(b) show plots of phonon intensity maps calculated along the same wave-vector path as for harmonic phonon curves. Each band consists of 100 phonon curves, but there are so many overlapping peaks that the information becomes obscure. Having 6000 modes for each wave vector **k**, one may construct histograms of all anharmonic peaks. Applying the projection method, Eqs. (14) and (16) one could have separated the spectra to all 60 anharmonic peaks. As examples we plot anharmonic peaks of B_{1g} and A_g symmetry on Figs. 3(d), 4(d), and 5. The spectra do not resemble the Lorentzian functions. At higher frequencies the centers of the peaks are very sharp, while in the low-intensity part the peaks become quite wide. Peaks at lower frequencies have irregular shapes. This could be due to insufficient sampling. Nevertheless, an estimate of the widths of B_{1g} and A_g peaks leads on average to 1.4 and 1.1 THz at $T = 2300$ K, and 0.9 and 0.6 THz at $T = 800$ K. These quantities could be compared with results of previous DFT works on $MgSiO_3$. Figure 1(b) of Ref. [11] refers to the linewidths of about 0.6 THz for three peaks with frequency close to 10.0 THz at $T = 700$ K, and, Figs. 2(g)–2(i) show linewidths of about 0.18 THz for peaks in the range from 7.44 to 15.3 THz at similar conditions. Figure 5(b) of Ref. [13] presents inverse anharmonic times at $T = 300$ K, $P = 24.1$ GPa, which suggests linewidths of anharmonic peaks from about 0.5 to 4.0 THz for phonon frequencies from an interval range of 5–25 THz, respectively. Figure 1(b) of Ref. [40] suggests a variation of linewidths at $T = 300$ K from 0.6 to 2.0 THz for phonon frequencies from an interval of 5–25 THz, respectively. The cited results are compatible with each other and similar to the results provided by the present approach.

C. Magnesium diboride MgB_2

MgB_2 becomes a superconductor at 39 K [45]. From deep studies of this material have emerged a phonon-mediated superconducting mechanism with moderate electron-phonon coupling [46–49] and anharmonicity [46,50,51]. The Raman spectroscopy has shown that the optical mode E_{2g} is strongly damped [52]. The inelastic x-ray-scattering measurement of

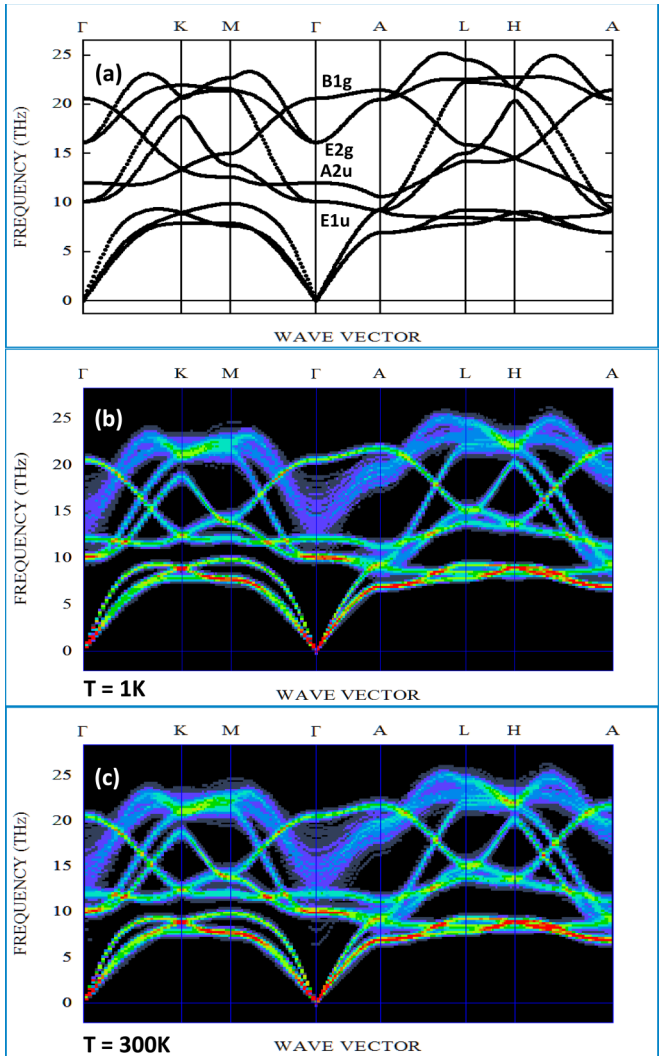

FIG. 6. MgB_2 phonon-dispersion curves plotted along Γ-K-M-Γ-A-L-H-A wave-vector path. E_{1u}, A_{2u}, E_{2g}, and B_{1g} are the irreducible representation of modes at Γ. (a) Harmonic phonon-dispersion relations. (b),(c) Anharmonic phonon maps created from averaging over 200 different sets of DP's at $T = 1$ K and $T = 300$ K, respectively.

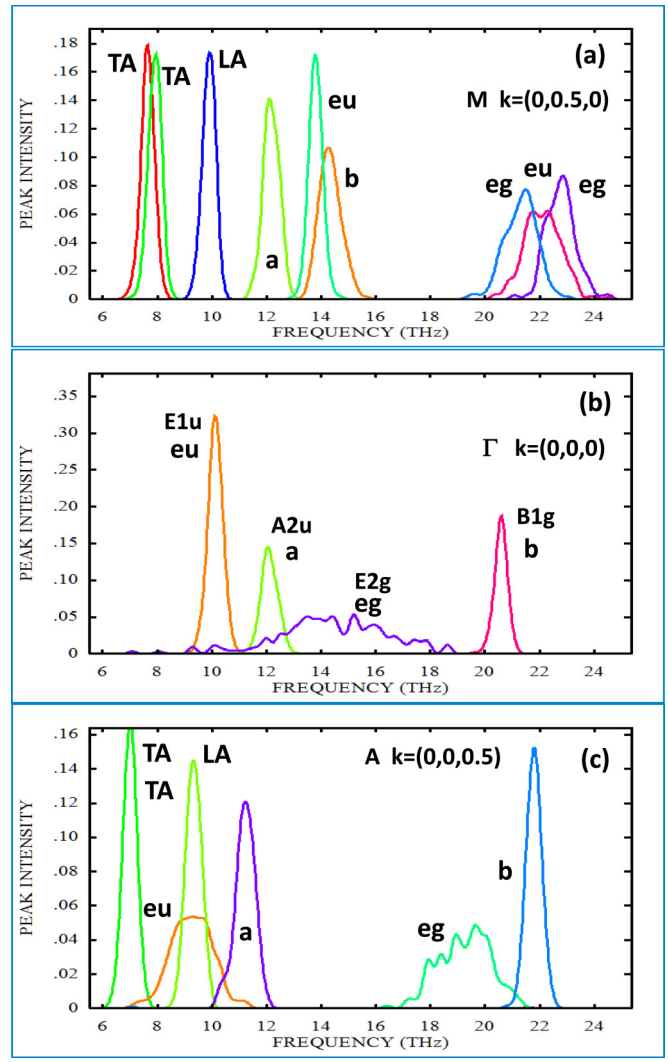

FIG. 7. MgB_2 anharmonic peaks plotted at (a) M, (b) Γ, and (c) A high-symmetry points in reciprocal space for $T = 1$ K. Labels a, b, eg, and eu correspond to notations of modes used in Table I.

phonon-dispersion curves revealed phonon broadening of the E_{2g} peak at Γ [53]. Anomalous broadening of phonon branches, extending from this E_{2g} along Γ-A and Γ-M directions, was also observed. Phonon damping can be caused by electron-phonon coupling and/or phonon-phonon interaction. Comparison of the *ab initio* quantum-mechanical calculations of the two types of interactions [53] established that the dominant contribution to the linewidth of E_{2g} is provided by the electron-phonon coupling [54,55].

MgB_2 crystallizes in the $P6/mmm$ space group. The optimization of the structure was performed in a rhombohedral supercell with 36 atoms, and 4×4×4 k-point mesh. The hexagonal lattice constants are equal to $a = 3.70$ Å, and $c = 3.52$ Å. To determine the harmonic phonon-dispersion curves it was necessary to calculate 12 lists of the HF forces for the $+/-$ displacements of nonequivalent Mg and B atoms. The resulting harmonic phonon-dispersion curves are plotted along Γ-K-M-Γ-A-L-H-A path [Fig. 6(a)]. At the Γ point they are indexed by irreducible representations of the point group $6/mmm$, where A_{2u}, B_{1g} and E_{2g}, E_{1u} are single and double degenerate modes, respectively.

At $T = 1$ K and $T = 300$ K the 200 DP's were generated. The atomic displacements at $T = 1$ K, corresponding to zero-temperature fluctuations $\bar{X}_i = \sqrt{\langle U_x U_x \rangle}$, $\bar{Z}_i = \sqrt{\langle U_z U_z \rangle}$, Eq. (13), were $\bar{X}_{Mg} = 0.0511$ Å, $\bar{Z}_{Mg} = 0.0516$ Å, and $\bar{X}_B = 0.0524$ Å, $\bar{Z}_B = 0.0595$ Å for Mg and B atoms, respectively. The computed 200 HF lists provided 200 sets of phonon-dispersion curves. Sorting phonon modes along the frequency axis determines a histogram. Amplitudes of the histogram bins, converted to colors, gave the intensity map as shown in Figs. 6(b) and 6(c). There are visible wide phonon bands, which include the phonon E_{2g} mode at Γ. The selected histograms, for wave vectors $\mathbf{k} = M$, $\mathbf{k} = \Gamma$, $\mathbf{k} = A$, with spline smoothed peaks, are displayed in Fig. 7. Data of optic phonons for the wave vectors of $\mathbf{k} = M$, Γ, and A are collected in Table I. It shows that the largest phonon linewidth occurs for

TABLE I. Calculated linewidth $\Gamma_{\mathbf{k},j}$ (THz) and estimated value of electron-phonon coupling constant $\lambda_{\mathbf{k},j}$, Eq. (17), at wave vectors $\mathbf{k} = M$, Γ, and A and phonon frequencies $\omega_{\mathbf{k},j}$ (THz) due to common phonon-phonon and electron-phonon interactions for MgB_2 at $T = 1$ K. In column of "Mode j" irreducible representations at Γ are given.

Mode j	$\omega_{M,j}$	$\Gamma_{M,j}$	$\lambda_{M,j}$	$\omega_{\Gamma,j}$	$\Gamma_{\Gamma,j}$	$\lambda_{\Gamma,j}$	$\omega_{A,j}$	$\Gamma_{A,j}$	$\lambda_{A,j}$
$E_{1u}(eu)$	14.3	1.08	0.57	10.1	0.58	0.62	9.3	1.79	2.25
$E_{1u}(eu)$	21.3	1.42	0.34	10.1	0.58	0.62	9.3	1.79	2.25
$A_{2u}(a)$	12.2	0.65	0.47	12.1	0.68	0.50	11.2	0.84	0.73
$E_{2g}(eg)$	22.1	1.75	0.39	14.4	**4.84**	**2.53**	19.3	2.28	0.66
$E_{2g}(eg)$	22.8	1.42	0.30	14.4	**4.84**	**2.53**	19.3	2.28	0.67
$B_{1g}(b)$	13.8	0.55	0.37	20.6	0.52	0.13	21.7	0.71	0.16

the E_{2g}, and reads 4.84 THz, and such a wide band extends over the whole wave-vector path displayed on the map [Fig. 6(b)]. The anharmonic linewidth at Γ was evaluated using the linear-response theory and the $(2n + 1)$ theorem for metals [53], and hence at Γ the anharmonic linewidths are equal to 0.039 THz at $T = 0$ K and 0.294 THz at $T = 300$ K, much less than the presently calculated value of 4.84 THz. This suggests that the main source of broadening is the electron-phonon coupling. It is obvious that our calculated linewidths contain both anharmonic contributions: tiny from phonon-phonon and dominant from electron-phonon interactions. At present the two contributions cannot be separated.

One may find the electron-phonon coupling $\lambda(\mathbf{k}, j)$ from Allen's linewidth expression [54]:

$$\lambda(\mathbf{k}, j) = \frac{\Gamma(\mathbf{k}, j)}{2\pi N(0)\omega^2(\mathbf{k}, j)}, \tag{17}$$

where $N(0) = 0.001\,464$ states/MbB_2 THz spin is the density of states at the Fermi level. Hence, the electron-phonon coupling for E_{2g} reads $\lambda = 2.53$. The computed data are listed in Table I for the exact wave vectors.

This linewidth of the E_{2g} mode is comparable with the magnitude of 4.92 THz of the similar mode at A wave vector measured with x rays [53].

The question of how the electron-phonon coupling is related to the linewidth of the E_{2g} phonon has been widely discussed in Refs. [55–59]. It was pointed out that the large increase of the Raman linewidth of E_{2g} symmetry between 40 and 300 K has no equivalence in the x-ray inelastic spectra. Indeed, the x-ray inelastic spectra show that the E_{2g} phonon linewidth along the Γ-A direction remains essentially temperature independent in the above-mentioned temperature range [56]. However, recent measurements of the temperature dependence of the E_{2g} peak up to $T = 750$ K showed a severe variation of the Raman linewidth. The peak behavior was successfully calculated taking into account the *ab initio* renormalization of electronic structure due to electron-phonon coupling [60].

Similar calculations for temperature $T = 300$ K, which involve larger displacements, namely $\bar{X}_{Mg} = 0.0706$ Å, $\bar{Z}_{Mg} = 0.0726$ Å, and $\bar{X}_B = 0.0603$Å, $\bar{Z}_B = 0.0723$ Å for Mg and B atoms, respectively, lead to a similar intensity map, Fig. 6(c) with, perhaps, a slightly larger linewidth of phonon peaks. The broad phonon band, which crosses the E_{2g} mode at Γ, is present.

IV. CONCLUSIONS AND DISCUSSIONS

The above formulated method proposes to probe the anharmonic potential-energy landscape by a series of atomic displacement configurations. Each configuration represents a fluctuation similar to collection of phonons. However, contrary to the molecular dynamic technique, the dynamical evolution of these fluctuations does not need to be studied explicitly. Instead, a series of atomic displacement configurations is generated. For each fixed atomic configuration the electronic states are minimized, and then, for this configuration, the list of all HF forces $\mathcal{F}_{\mathcal{A}}{}^{(i)}$ is found. (It is in contrast to the conventional perturbation approach, where anharmonic force constants are calculated by optimization of configurations with only three or four atoms displaced, while leaving the remaining atoms at equilibrium.) Perhaps the minimization of electronic energy of the displaced configuration DP involving all atoms is essential for achieving the correct HF forces, which lead, if present, to describing the strong electron-phonon coupling. The forces $\mathcal{F}_{\mathcal{A}}{}^{(i)}$ are used to calculate the bands of phonon-dispersion curves [24] guided by Eq. (11), in which the harmonic dispersion curves play a reference role.

Within symmetry consideration, the irreducible representations of the phonon modes are determined by the crystallographic space group. The transformation of the phonon polarization vectors decides about the irreducible representation related with a considered phonon mode. Notice that the same transformation can be applied to all DP's, $i = 1, 2, 3, \ldots N$, hence, to all phonon curves belonging to the same band and the same wave vector $\mathbf{k}$. From this follows that the whole anharmonic peak area really belongs by the same irreducible representation.

The present method applies some similar ideas as used in the SCAILD [14,15,61] approach. The common features are that this approach assumes the systems to be confined to a supercell, which is filled with possible commensurate phonon waves, next used to calculate modified phonon frequencies, and amplitudes for the subsequent consecutive cycles, till the procedure converges. During this self-consistency procedure the HF forces are found via a DFT code. The results deliver renormalized phonon-dispersion curves, and even the phonon linewidth in a form of the Gaussian [61]. Based on similar ideas, another self-consistent method is proposed: SSCHA [16].

In the method proposed in this paper the supercell is also filled with all possible commensurate phonon waves, but additionally we make use of the phases of every phonon, which remarkably increases the amount of possible atomic configurations, DP's. Each atomic configuration is treated as a perturbation in the sense of the SVD procedure, as shown in Eq. (11). (The perturbation does not have expansional character.) Then, phonon frequencies and polarization vectors are calculated once for all created DPs. It must be stressed that the essential point is the SVD procedure, which not only finds phonon frequencies, but also provides the least-square fitting of values of all force constants to the actual configurations of atoms, simultaneously conserving the crystal symmetry properties. Currently the unstable phonon phenomena and the self-consistent procedure are not considered.

Several theoretical works have given estimates of the phonon frequency and shift in MgB_2 using direct, or frozen phonon approaches. See [57] for references. There it is stated that the perturbation theory with third-, fourth-, and higher-order terms may require us to go beyond the Born-Oppenheimer approximation [62]. Indeed, such a typical calculation assumes that phonons are static perturbations, where nonactive atoms remain at equilibrium positions. In the present method the forces ${\mathcal{F}_{\mathcal{A}}}^{(i)}$, used in Eq. (11), are calculated at a fixed displaced configuration of all atoms (DP), and the electronic energy relaxes to the optimized state, at which the HF forces ${\mathcal{F}_{\mathcal{A}}}^{(i)}$ are collected.

The method offers a high degree of computing parallelization, since the electronic relaxation of each displacement configuration, which leads to HF forces ${\mathcal{F}_{\mathcal{A}}}^{(i)}$, can be done simultaneously. Moreover, each such run is limited to a single ionic loop, hence the CPU time could be rather short, even if several hundreds of HF force lists are required.

ACKNOWLEDGMENTS

The author would like to acknowledge discussions with M. Krisch, E. Wimmer, W. Wolf, P. Piekarz, A. M. Oleś, P. Jochym, J. Łażewski, M. Sternik, and A. Ptok.

[1] R. A. Cowley, Rep. Prog. Phys. **31**, 123 (1968).
[2] A. A. Maradudin and A. E. Fein, Phys. Rev. **128**, 2589 (1962).
[3] G. Deinzer, G. Birner, and D. Strauch, Phys. Rev. B **67**, 144304 (2003).
[4] K. Esfarjani and H. T. Stokes, Phys. Rev. B **77**, 144112 (2008).
[5] K. H. Michel, S. Costamagna, and F. M. Peeters, Phys. Rev. B **91**, 134302 (2015).
[6] T. H. K. Barron and M. L. Klein, in *Dynamical Properties of Solids*, edited by G. K. Horton and A. A. Maradudin (North-Holland, Amsterdam, Elsevier, New York, 1974), Vol. 1, p. 391.
[7] N. R. Werthamer, Phys. Rev. B **1**, 572 (1970).
[8] W. Götze and K. H. Michel, in *Dynamical Properties of Solids* (Ref. [6]), Vol. 1, p. 498.
[9] T. Sun, D. B. Zhang, and R. M. Wentzcovitch, Phys. Rev. B **89**, 094109 (2014).
[10] D. B. Zhang, P. B. Allen, T. Sun, and R. M. Wentzcovitch, Phys. Rev. B **96**, 100302 (2017).
[11] D. B. Zhang, T. Sun, and R. M. Wentzcovitch, Phys. Rev. Lett. **112**, 058501 (2014).
[12] A. France-Lanord, P. Soukiassian, Ch. Glattli, and E. Wimmer, Phys. Rev. Appl. **7**, 034030 (2017).
[13] N. Ghaderi, D.-B. Zhang, H. Zhang, J. Xian, R. M. Wentzcovitch, and T. Sun, Sci. Rep. **7**, 5417 (2017).
[14] P. Souvatzis, O. Eriksson, M. I. Katsnelson, and S. P. Rudin, Phys. Rev. Lett. **100**, 095901 (2008).
[15] H.-Y. Zhang, Z.-W. Niu, L.-C. Cai, X.-R. Chen, and F. Xi, Comput. Mater. Sci. **144**, 32 (2018).
[16] I. Errea, M. Calandra, and F. Mauri, Phys. Rev. B **89**, 064302 (2014).
[17] O. Hellman, I. A. Abrikosov, and S. I. Simak, Phys. Rev. B **84**, 180301 (2011).
[18] O. Hellman and I. A. Abrikosov, Phys. Rev. B **88**, 144301 (2013).
[19] T. Tadano and S. Tsuneyuki, J. Phys. Soc. Jpn. **87**, 041015 (2018).
[20] H. Horner, Z. Phys. **205**, 72 (1967).
[21] J. J. Plata, P. Nath, D. Usanmaz, J. Carrete, C. Toher, M. de Jong, M. Asta, M. Fornari, M. B. Nardelli, and S. Curtarolo, npj Comput. Mater. **3**, 45 (2015).
[22] T. Tadano and S. Tsuneyuki, Phys. Rev. B **92**, 054301 (2015).
[23] W. Li, J. Carrete, N. K. Katcho, and N. Mingo, Comput. Phys. Commun. **185**, 1747 (2014).
[24] K. Parlinski, Z.-Q. Li, and Y. Kawazoe, Phys. Rev. Lett. **78**, 4063 (1997).
[25] G. Kresse, J. Furthmüller, and J. Hafner, Europhys. Lett. **32**, 729 (1995).
[26] A. A. Maradudin, in *Dynamical Properties of Solids* (Ref. [6]), Vol. 1, p. 1.
[27] W. H. Press, S. A. Teukolsky, W. T. Vetterling, and B. P. Flannery, in *Numerical Recipes* (Cambridge University Press, Cambridge, England, 1992), p. 670.
[28] G. W. Stewart, in *SVD and Signal Processing, II: Algorithms, Analysis and Applications*, edited by R. J. Vaccaro (Elsevier Science, Amsterdam, 1991), p. 99.
[29] E. Candès and M. Wakin, IEEE Signal Proc. Mag. **25**, 21 (2008).
[30] F. Zhou, W. Nielson, Y. Xia, and V. Ozoliņš, Phys. Rev. Lett. **113**, 185501 (2014).
[31] G. Grimvall, in *Thermophysical Properties of Materials* (Elsevier Science, Amsterdam, 1999), p. 121.
[32] P. Debye, Ann. Phys. **348**, 49 (1913).
[33] H. Ott, Ann. Phys. **415**, 169 (1935).
[34] G. Kresse and J. Furthmüller, Phys. Rev. B **54**, 11169 (1996); Comput. Mater. Sci. **6**, 15 (1996).
[35] K. Parlinski, in *Neutrons and Numerical Methods*, edited by M. R. Johnson, G. J. Kearley, and H. G. Büttner, AIP Conf. Proc. No. 479 (AIP, Melville, NY, 1999), pp. 121–126.
[36] A. D. B. Woods and S. H. Chen, Solid State Commun. **2**, 233 (1964).
[37] A. Larose and B. N. Brockhouse, Can. J. Phys. **54**, 1819 (1976).
[38] W. Kohn, Phys. Rev. Lett. **2**, 393 (1959).
[39] S. L. Daraszkiewicz, Y. Giret, H. Tanimura, D. M. Duffy, A. L. Shluger, and K. Tanimura, Appl. Phys. Lett. **105**, 023112 (2014).
[40] H. Dekura, T. Tsuchiya, and J. Tsuchiya, Phys. Rev. Lett. **110**, 025904 (2013).
[41] H. Horiuch, E. Ito, and D. J. Weidner, Am. Mineral. **72**, 357 (1987).
[42] E. Ito and Y. Matsui, Earth Planet Sci. Lett. **38**, 443 (1978).
[43] Y. Kudoh, E. Ito, and H. Takeda, Phys. Chem. Miner. **14**, 350 (1987).
[44] K. Parlinski and Y. Kawazoe, Eur. J. Phys. B **16**, 49 (2000).
[45] J. Nagamatsu, N. Nakagawa, T. Muranaka, Y. Zenitani, and J. Akimitsu, Nature (London) **410**, 63 (2001).
[46] A. Y. Liu, I. I. Mazin, and J. Kortus, Phys. Rev. Lett. **87**, 087005 (2001).
[47] J. M. An and W. E. Pickett, Phys. Rev. Lett. **86**, 4366 (2001).
[48] J. Kortus, I. I. Mazin, K. D. Belashchenko, V. P. Antropov, and L. L. Boyer, Phys. Rev. Lett. **86**, 4656 (2001).

[49] Y. Kong, O. V. Dolgov, O. Jepsen, and O. K. Andersen, Phys. Rev. B **64**, 020501 (2001).
[50] T. Yildirim, O. Gulseren, J. W. Lynn, C. M. Brown, T. J. Udovic, Q. Huang, N. Rogado, K. A. Regan, M. A. Hayward, J. S. Slusky, T. He, M. K. Haas, P. Khalifah, K. Inumaru, and R. J. Cava, Phys. Rev. Lett. **87**, 037001 (2001).
[51] L. Boeri, G. B. Bachelet, E. Cappelluti, and L. Pietronero, Phys. Rev. B **65**, 214501 (2002).
[52] J. Hlinka, I. Gregora, J. Pokorny, A. Plecenik, P. Kus, L. Satrapinsky, and S. Benacka, Phys. Rev. B **64**, 140503(R) (2001).
[53] A. Shukla, M. Calandra, M.d'Astuto, M. Lazzeri, F Mauri, C. Bellin, M. Krisch, J. Karpinski, S. M. Kazakov, J. Jun, D. Daghero, and K. Parlinski, Phys. Rev. Lett. **90**, 095506 (2003).
[54] P. B. Allen, Phys. Rev. B **6**, 2577 (1972).
[55] J. Menendez and M. Cardona, Phys. Rev. B **29**, 2051 (1984).
[56] M d'Astuto, M. Calandra, S. Reich, A. Shukla, M. Lazzeri, F. Mauri, J. Karpinski, N. D. Zhigadlo, A. Bossak, and M. Krisch, Phys. Rev. B **75**, 174508 (2007).
[57] M. Calandra, M. Lazzeri, and F. Mauri, Phys. C (Amsterdam, Neth.) **456**, 38 (2007).
[58] E. Cappelluti, Phys. Rev. B **73**, 140505(R) (2006).
[59] M. Calandra and F. Mauri, Phys. Rev. B **71**, 064501 (2005).
[60] Yu. S. Ponosov and S. V. Streltsov, Phys. Rev. B **96**, 214503 (2017).
[61] P. Souvatzis, J. Phys.: Condens. Matter **23**, 445401 (2011).
[62] M. Born and R. Oppenheimer, Ann. Phys. **389**, 457 (1927).